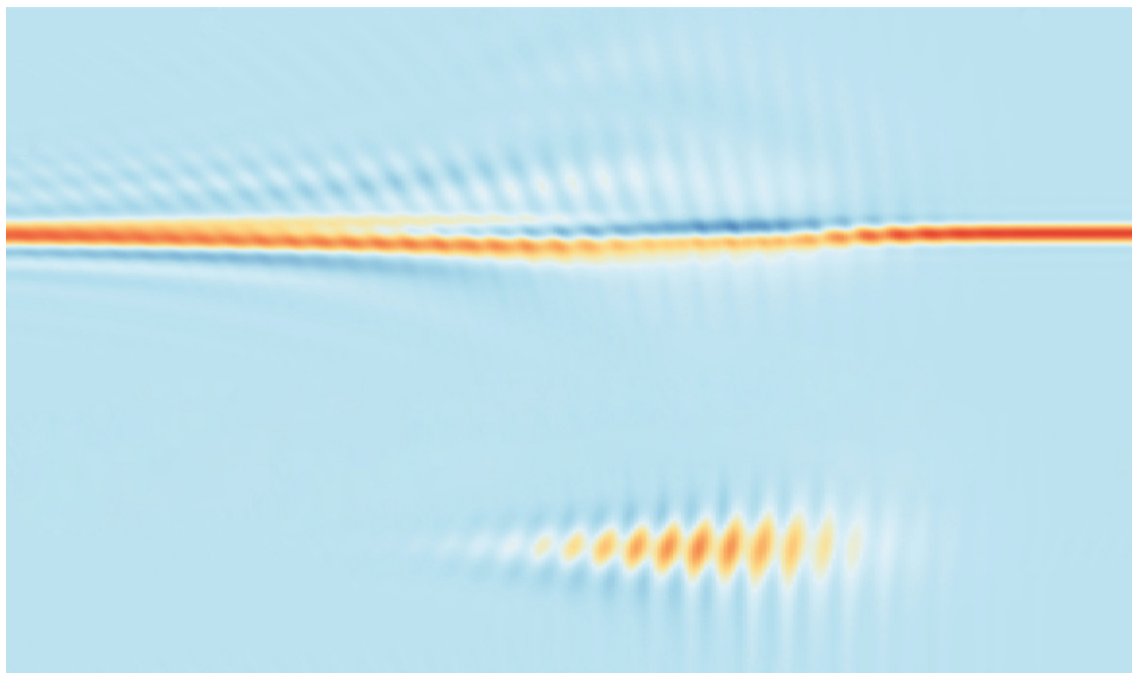


ELECTRON DYNAMICS: A NOVEL NUMERICAL
APPROACH AND ATTOSECOND TRANSIENT
ABSORPTION SPECTROSCOPY



PART A PROGRESS RAPPORT

JENS EGEBJERG BÆKHØJ (20082846)

MAIN SUPERVISOR: LARS BOJER MADSEN

MAY 2014

DEPARTMENT OF PHYSICS AND ASTRONOMY
GRADUATE SCHOOL OF SCIENCE AND TECHNOLOGY
AARHUS UNIVERSITY

Preface

This progress report contains a brief overview of the work done during part A of my Ph.D. at the Department of Physics and Astronomy, Aarhus University. The backbone of the thesis is chapter 2 and chapter 3. The structure of chapter 2 is similar to the structure in ref. [1] published March 2014, but text and calculations has been modified to highlight central ideas and physical content. Chapter 3 consists of unpublished material. The content of this chapter has been the main focus of my research the last few months.

Units and notation

Atomic units will be used throughout this report unless explicitly stated otherwise. We use the standard Dirac notation, including $\langle \dots \rangle$ for inner products in a Hilbert space.

Acknowledgments

I would like to thank my office mates Jens and Christian for fruitful discussions throughout the part A of my Ph.D. I appreciate the cooperation with my co-supervisor Oleg I. Tolstikhin, since he has helped shaping me as a theoretical physicist. Finally I would like to thank Lars for his invaluable supervision. Lars is always ready to help, no matter the nature of the problem, and you always fell welcome.

Contents

Preface	I
Units and notation	I
Acknowledgments	I
Contents	i
1 Introduction	1
2 ‘Slow’ Time Discretization	3
2.1 Introduction	3
2.2 Adiabatic states and the Born-Fock equations	4
2.3 Construction of the STD propagator	5
2.4 Illustrative examples	9
2.4.1 Implementation	9
2.4.2 Hydrogen atom in a pulsed laser field	10
2.4.3 Proton-hydrogen collisions	12
2.5 Conclusion	15
3 Attosecond Transient Absorption Spectroscopy	16
3.1 Introduction	16
3.2 Theory	17
3.3 Implementation and Results	18
3.3.1 Fixed nuclei calculations	19
3.3.2 Moving nuclei calculations	22
3.4 Conclusion	24
4 Further plans	25
A Discrete Variable Representation (DVR)	27
A.1 A short introduction to the DVR basis	27
A.2 Field parameters	29
Bibliography	31

Introduction

The human brain can process 10 to 12 separate images from the eye per second. This allows us to follow dynamics on a millisecond time scale, which is the natural time scale for the macroscopic everyday world. In experiments with atoms and molecules, the system of eyes and brain has been replaced by a system of one or several laser-pulses and detectors, allowing temporal resolution on the timescale of the shortest laser pulse involved. Rapid development in laser technology, has lead to shorter and shorter laser pulses, and in 2001 the first laser pulse with a duration in the attosecond regime was produced [2]. The production of attosecond pulses is the first step in designing experiments able to follow electron dynamics on its natural time scale. In this thesis we will discuss a particularly successful group of experiments. As opposed to longer laser pulses, attosecond pulses are characterized by relatively low intensities and are therefore often well described by perturbation theory. The femtosecond pulses frequently used to produce attosecond pulses, on the other hand, often have field strengths comparable to the Coulombic force experienced by electrons bound in atomic or molecular systems.

Traditionally, not much attention was paid to the development of methods capable of solving the time-dependent Schrödinger equation (TDSE)

$$i\partial_t|\Psi(t)\rangle = H(t)|\Psi(t)\rangle, \quad (1.1)$$

through which the Hamiltonian $H(t)$ controls the dynamics of the corresponding quantum mechanical system, represented by the state $|\Psi(t)\rangle$. Instead, time-dependent problems were treated by appropriate boundary conditions for stationary solutions, and using time-dependent perturbation theory. However, it is clear that the forces experienced by electrons during e.g. one of the femtosecond pulses described above, are by no means in the perturbative regime. Together with the ever increasing computer power, this problem has lead to a long list of numerical schemes for solving the TDSE. Among the most efficient are the Crank-Nicolson scheme [3], the fast-Fourier-transform split-step-operator method [4], the Chebyshev scheme [5], and the iterative Lanczos propagator [6]. All of these methods have found numerous applications in both physics and chemistry, but non of them are universal. Considering the physical domain of the problem, one must chose the method making the best compromise between precision and computational cost. In Chapter 2 we propose a method constructed to be particularly efficient, when the system under consideration evolves slowly in time. It turns out, however, that the method works well also for faster evolving systems, as long as the evolution is smooth in time.

In the beginning of this chapter, I stated that experiments can reach temporal resolution on the time scale of the shortest pulse involved. To obtain temporal resolution in the sub-femtosecond region, however, is by no means trivial. Even when an attosecond pulse has been produced, which is a difficult task on its own, there is no way this pulse, or dynamics

initiated by the pulse, can be followed directly by electronic devices. One solution to this problem is to build in a measurable time variable in the laser field itself. In *pump-probe* experiments this variable is a time delay between two laser pulses. A pump pulse initiates a dynamical process in some target, and after a time delay a probe pulse takes a 'snapshot' of the system. Since the pump pulse defines a zero-point in time, a scan over a range of different time delays will give information about the temporal evolution of the process initiated by the pump pulse.

The effect of a probe pulse in pump-probe experiments can be analyzed following two different approaches. The first approach is to monitor effects in the target system, initiated by the probe pulse itself. The most prominent example in attosecond physics is attosecond streaking. In attosecond streaking the probe pulse ionizes the target perturbed by the pump pulse, and the spectrum of photoelectrons is recorded [7], [8]. The second approach is to monitor the back-action from the target on the probe pulse itself. The method discussed in chapter 3 is an example of the second approach. Both approaches measure the temporal evolution of the system in an indirect way, by considering the probe pulse in a temporal frame set by the pump pulse. It is therefore vital to the temporal resolution of the experiment, that the probe pulse is short compared to the process of interest¹. In chapter 3 we investigate *attosecond transient absorption spectroscopy* (ATAS), where the transmission of an attosecond probe pulse is recorded. We develop a simple, but efficient theory to calculate the intensity spectrum of the probe pulse, after its propagation through a target. This theory is applied to two models of the H_2^+ -molecule; one where the nuclei are fixed and one where they are allowed to move. The motivation for this is to investigate the effect of nuclear motion on the intensity spectrum.

¹Depending on the nature of the process, the length of the pump pulse can be just as important.

'Slow' Time Discretization

2.1 Introduction

A frequently used tool in computational atomic and molecular physics, is the expansion of a quantum state $|\Psi\rangle$ in a complete set $\{|\varphi_i(t)\rangle | i = 1, \dots, n\}$

$$|\Psi\rangle = \sum_{i=1}^n c_i |\varphi_i\rangle, \quad (2.1)$$

where $c_i = \langle \varphi_i | \Psi \rangle$. For the problems considered in this thesis, equation (2.1) will be exact only in the limit of $n \rightarrow \infty$. In practical calculations, however, one always work with a finite basis and the sum must be truncated. The number of basis states needed for a desired precision depends on how well the basis states $|\varphi_1\rangle, |\varphi_2\rangle, \dots, |\varphi_n\rangle$ mimics the physics of $|\Psi\rangle$, and a clever choice of basis can be of great importance.

Temporal evolution of a quantum state is governed by the TDSE (equation (1.1)). The simplest possible situation is the evolution of a state, evolving under a time-independent Hamiltonian. In this case it will be natural to chose the (time-independent) eigenstates of the Hamiltonian as basis states, since there will be no coupling between such states under time evolution, and each term in the expansion (2.1) will evolve independently. When the Hamiltonian $H(t)$ is not time-independent, but changes on a time scale much longer then the intrinsic time scales of the system¹, the system is said to evolve *adiabatically* and obeys the *adiabatic theorem*. The adiabatic theorem states that if a quantum state $|\Psi(t)\rangle$ is expanded in the basis of instantaneous eigenstates of $H(t)$, and the corresponding system changes adiabatically, there will be no transfer of population between basis states during propagation in time². We refer to the instantaneous eigenstates of $H(t)$ as *adiabatic states* [9]. The expansion of an adiabatically evolving quantum state $|\Psi(t)\rangle$ in adiabatic states, will therefore also evolve in time without coupling between basis states. If we relax the requirement that $H(t)$ changes adiabatically, we will introduce couplings between the adiabatic basis states (non-adiabatic couplings). Even though one would expect these non-adiabatic couplings to be small for slowly varying systems, it turns out that they lead to major numerical difficulties, as will be discussed in section 2.2 and 2.4.

It is practical to introduce an operator $U(t_b, t_a)$ that propagate a solution $|\Psi(t)\rangle$ of the TDSE from an initial time t_a to a later time t_b ,

$$|\Psi(t_b)\rangle = U(t_b, t_a) |\Psi(t_a)\rangle. \quad (2.2)$$

¹We here discuss the limit where $H(t)$ is an infinity slowly varying function of time.

²We assume that the spectrum of $H(t)$ is discrete and non-degenerate for all times. The assumption about non-degeneracy is only for the clarity of the argument, and the method developed in this chapter can also treat systems with degenerate states.

The operator $U(t_b, t_a)$ is referred to as a time propagator. The main purpose of this chapter is to explicitly construct a time propagator from the TDSE, which enjoys the advantages of a representation in adiabatic states, but circumvents the problems of non-adiabatic couplings. This is done using the principles of *slow variable discretization* (SVD), used originally in ref. [10] to solve the time-independent Schrödinger equation. We will refer to our new method as *slow time discretization* (STD).

Section 2.2 will introduce the adiabatic states in a more thorough manner. Hereafter we set up the Born-Fock equations as a starting point for the discussion of non-adiabatic couplings and their numerical consequences. In section 2.3 it is shown how the problems of non-adiabatic couplings can be avoided in the STD formulation, and how this enable us to implement an efficient algebraic representation of the time propagator. Section 2.4 will present two simple, but illustrative examples of calculations carried out using the STD propagator. Finally section 2.5 conclude this chapter.

2.2 Adiabatic states and the Born-Fock equations

For a system evolving in time according to the Hamiltonian $H(t)$, the adiabatic states at time t are defined as the eigenstates of the instantaneous Hamiltonian

$$H(t)|\varphi_\nu(t)\rangle = E_\nu(t)|\varphi_\nu(t)\rangle, \quad (2.3)$$

where $E_\nu(t)$ are the adiabatic energies and the index $\nu = 1, \dots, N_{\text{ch}}$ enumerates the adiabatic channels. It is assumed that the spectrum of $H(t)$ is purely discrete, and that $H(t)$ is hermitian ($H(t) = H^\dagger(t)$); otherwise the system can be arbitrary. Finally, we assume that the adiabatic states form an orthonormal basis for all times

$$\langle\varphi_\nu(t)|\varphi_\mu(t)\rangle = \delta_{\nu\mu}, \quad (2.4)$$

and becomes complete in the limit where the number of basis states N_{ch} goes to infinity

$$\lim_{N_{\text{ch}} \rightarrow \infty} \sum_{\nu=1}^{N_{\text{ch}}} |\varphi_\nu(t)\rangle\langle\varphi_\nu(t)| = 1. \quad (2.5)$$

The idea of expanding a solution of the TDSE $|\Psi(t)\rangle$, in adiabatic states

$$|\Psi(t)\rangle = \sum_{\mu=1}^{N_{\text{ch}}} f_\mu(t)|\varphi_\mu(t)\rangle \quad (2.6)$$

dates all the way back to 1928 where M. Born and V. Fock published the first paper on the subject [11]. Substitution of equation (2.6) into the TDSE (equation (1.1)) and projection from the left onto the bra $\langle\varphi_\nu(t)|$, leads to the Born-Fock equations for the unknown functions $f_\mu(t)$

$$i\partial_t f_\nu(t) + i \sum_{\mu=1}^{N_{\text{ch}}} P_{\nu\mu}(t) f_\mu(t) = E_\nu(t) f_\nu(t), \quad (2.7)$$

where

$$P_{\nu\mu}(t) = \langle\varphi_\nu(t)|\partial_t\varphi_\mu(t)\rangle, \quad (2.8)$$

is the matrix of non-adiabatic couplings. At first equation (2.7) seems to be an efficient tool for numerical evaluation of the functions $f_\mu(t)$, and thereby of the state $|\Psi(t)\rangle$. However, the nature of the adiabatic states are such that the non-adiabatic couplings can be extremely

localized in time, so even though the couplings are weak on average, locally they can be extremely strong. One way to realize this, is to consider the adiabatic energy curves. When the Hamiltonian $H(t)$ of a system changes with time, it leads to a change in the adiabatic energies and in some areas, the energies of two adiabatic channels can come close. When two energy curves come close, there are two possible scenarios; the energy curves can cross or they can preform an *avoided crossing*. During an avoided crossing the corresponding adiabatic states interact to keep the energy curves separated, and this interaction can be very strong and very localised. We will not go into detail with the physics of avoided crossings in the adiabatic energy curves, but only note that these avoided crossings have many similarities with the avoided crossings in electronic energy curves of diatomic molecules, as functions of the inter-nuclear distance. An analysis of the latter is made in [12], and generalisations hereof are possible. One should note, however, that the symmetry selection rules from the molecular case cannot be carried over directly, since in our case the symmetry of the potential can be different.

In the near-adiabatic case, the norm of the expansion coefficients $f_\mu(t)$ will not change much over time, not even near avoided crossings, but the rapid change in energy and particularly of $P_{V\mu}(t)$ will make a numerical evaluation very difficult; in the non-adiabatic case this evaluation is practically impossible since $f_\mu(t)$ itself also changes rapidly with time. In section 2.4 we show examples of avoided crossings of adiabatic energy curves, for a system used in our calculations.

2.3 Construction of the STD propagator

Provided that the Hamiltonian $H(t)$ is a smooth function of time, the solution $|\Psi(t)\rangle$ of the TDSE will evolve smoothly in time. We therefore expect the numerical problems in the evaluation of equation (2.7) to be a consequence of the adiabatic basis. Other (diabatic) bases could therefore be more suitable for the expansion of $|\Psi(t)\rangle$. However, in the case where our system is not evolving too fast, we still expect the adiabatic states to describe the spatial variables of the problem in a favorable way, and consequentially $|\Psi(t)\rangle|_{t=t'}$ can be expanded in few adiabatic states for any t' .

In any sufficiently short time interval, even if there are avoided crossings in it, the smooth function $|\Psi(t)\rangle$ can be accurately described by an expansion in a few temporal states. In this section, our approach will therefore be to treat time by an expansion in a temporal basis, and only hereafter treat the spatial degrees of freedom by an expansion in adiabatic states. For the temporal basis we use a so called *discrete variable representation* (DVR), since special properties of this basis enable us to construct an efficient algebraic representation of the time propagator. Appendix A contains a short introduction to DVR functions.

We consider the solution $|\Psi(t)\rangle$ to the TDSE on the time interval

$$t \in [t_a, t_b]. \quad (2.9)$$

To achieve the goal of an algebraic representation of the propagator $U(t_a, t_b)$, we extend the SVD method introduced in ref. [10] to the time-dependent case, with time treated as the 'slow' variable. First step in this approach is to treat the time dependence of $|\Psi(t)\rangle$. Let the functions $\pi_i(t), i = 1, \dots, N_{\text{DVR}}$ provide a basis in $L^2[t_a, t_b]$. This temporal basis is assumed to be orthonormal

$$(\pi_i | \pi_j) \equiv \int_{t_a}^{t_b} \pi_i^*(t) \pi_j(t) dt = \delta_{ij}, \quad (2.10)$$

and complete in the limit of infinitely many basis states

$$\lim_{N_{\text{DVR}} \rightarrow \infty} \sum_{i=1}^{N_{\text{DVR}}} \pi_i(t) \pi_i^*(t') = \delta(t - t'). \quad (2.11)$$

In addition, we assume that the temporal basis have the *pointwise* properties

$$\pi_i(t_j) = W_i \delta_{ij}, \quad (2.12)$$

$$(\pi_i | F(t) | \pi_j) = \int_{t_a}^{t_b} \pi_i^*(t) F(t) \pi_j(t) dt \approx F(t_i) \delta_{ij}, \quad (2.13)$$

where $t_i, i = 1, \dots, N_{\text{DVR}}$, are the abscissas of an associated quadrature, W_i is a coefficient related to the quadrature weight (see appendix A) and $F(t)$ is an arbitrary function. The pointwise properties of equations (2.12) and (2.13) are characteristic of a DVR basis. In appendix A we discuss general properties of the DVR basis, and show that the corresponding basis vectors have properties given in equations (2.10)-(2.13).

$|\Psi(t)\rangle$ is expanded in the set of temporal DVR functions $\pi_i(t), i = 1, \dots, N_{\text{DVR}}$

$$|\Psi(t)\rangle = \sum_{j=1}^{N_{\text{DVR}}} \pi_j(t) |\varphi_j\rangle. \quad (2.14)$$

It is important to note that the yet unknown functions $|\varphi_j\rangle$ in equation (2.14) are time-independent. These functions can therefore be expanded in an adiabatic basis, without the numerical problems resulting from propagating through avoided crossings of the energy curves. The property (2.12) suggests that we expand $|\varphi_j\rangle$ in the adiabatic basis $\{|\varphi_\mu(t)\rangle | \mu = 1, \dots, N_{\text{ch}}\}$ evaluated at the quadrature abscissas t_j

$$|\varphi_j\rangle = \sum_{\mu=1}^{N_{\text{ch}}} c_{j\mu} |\varphi_\mu(t_j)\rangle. \quad (2.15)$$

Combining equations (2.15) and (2.14) we obtain

$$|\Psi(t)\rangle = \sum_{j=1}^{N_{\text{DVR}}} \sum_{\mu=1}^{N_{\text{ch}}} c_{j\mu} \pi_j(t) |\varphi_\mu(t_j)\rangle. \quad (2.16)$$

We will refer to equation (2.16) as the STD expansion. Under the requirement that the STD expansion is converged with respect to both the number of temporal basis functions N_{DVR} and the number of adiabatic basis states N_{ch} , the $N_{\text{STD}} = N_{\text{DVR}} \times N_{\text{ch}}$ coefficients $c_{j\mu}$ completely determines the state $|\Psi(t)\rangle$ on the time interval (2.9).

To investigate the temporal development of the state $|\Psi(t)\rangle$, now given in the STD representation, we return to the TDSE. First we project the bra $\langle \pi_i | = \int_{t_a}^{t_b} \pi_i^*(t) dt$ defined in $L^2[t_a, t_b]$ (see equation (2.10)) onto the TDSE (equation (1.1)) to obtain

$$i \int_{t_a}^{t_b} \pi_i^*(t) \partial_t |\Psi(t)\rangle dt = \int_{t_a}^{t_b} \pi_i^*(t) H(t) |\Psi(t)\rangle dt. \quad (2.17)$$

Integration by parts, allows us to rewrite the left hand side (LHS) of equation (2.17)

$$i \int_{t_a}^{t_b} \pi_i^*(t) \partial_t |\Psi(t)\rangle dt = \frac{i}{2} \left(\pi_i^*(t) |\Psi(t)\rangle \Big|_{t_a}^{t_b} + \int_{t_a}^{t_b} [\pi_i^*(t) \partial_t - \partial_t \{\pi_i^*(t)\}] |\Psi(t)\rangle dt \right). \quad (2.18)$$

Equation (2.18) may not seem to be much of a simplification, but as we will see later this particular way of writing the LHS of equation (2.17) is actually a very important step in the derivation of the STD time propagator. Equation (2.18) is now inserted in equation (2.17)

$$\int_{t_a}^{t_b} \left(\frac{i}{2} [\pi_i^*(t) \partial_t - \partial_t \{\pi_i^*(t)\}] - \pi_i^*(t) H(t) \right) |\Psi(t)\rangle dt = -\frac{i}{2} \pi_i^*(t) |\Psi(t)\rangle \Big|_{t_a}^{t_b}, \quad (2.19)$$

and the STD expansion is inserted on the LHS

$$\sum_{j=1}^{N_{\text{DVR}}} \sum_{\mu=1}^{N_{\text{ch}}} \left[\frac{i}{2} (D_{ij} - D_{ji}^*) - \delta_{ij} H(t_i) \right] c_{j\mu} |\varphi_{\mu}(t_j)\rangle = -\frac{i}{2} \pi_i^*(t) |\Psi(t)\rangle \Big|_{t_a}^{t_b}, \quad (2.20)$$

where

$$D_{ij} = (\pi_i | \partial_t \pi_j) = \int_{t_a}^{t_b} \pi_i^*(t) \partial_t \pi_j(t) dt. \quad (2.21)$$

To obtain equation (2.20) we used the DVR property (2.13) with $F(t) = H(t)$. The approximation from equation (2.13) are therefore passed on to equation (2.20), and deserves a comment before we proceed. From properties of the Gaussian quadrature (see appendix A), it can be shown that equation (2.13) is exact when $F(t)$ is a polynomial of degree one or less. When this is not the case, the approximation will in general be better as the number of terms in the expansion of $F(t)$ in powers of t , sufficient for an accurate representation, becomes lower. However, for any $F(t)$ equation (2.13) is expected to converge fast towards the exact result, as the number of basis states is raised, provided that $F(t)$ is a *smooth* (infinitely differentiable) function of time. For an efficient numerical implementation, $H(t)$ must therefore vary smoothly in time, and preferably also slowly. As we will see in section 2.4 the slow variation of $H(t)$ is not essential, but the smoothness is.

We now project the bra $\langle \varphi_{\nu}(t_i) |$, corresponding to the ν 'th adiabatic state evaluated at the i 'th quadrature abscissa, onto equation (2.20) from the left

$$\sum_{j=1}^{N_{\text{DVR}}} \sum_{\mu=1}^{N_{\text{ch}}} \left[\frac{i}{2} (D_{ij} - D_{ji}^*) O_{iv,j\mu} - \delta_{ij} \delta_{\nu\mu} E_{\nu}(t_i) \right] c_{j\mu} = -\frac{i}{2} \pi_i^*(t) \langle \varphi_{\nu}(t_i) | \Psi(t) \rangle \Big|_{t_a}^{t_b}, \quad (2.22)$$

where

$$O_{iv,j\mu} = \langle \varphi_{\nu}(t_i) | \varphi_{\mu}(t_j) \rangle, \quad (2.23)$$

is the matrix of overlap elements between adiabatic basis states taken at different quadrature abscissas. To obtain equation (2.22) we used equations (2.3) and (2.4). The right hand side (RHS) of equation (2.22) contains the state $|\Psi(t)\rangle$ evaluated at the temporal end points t_a and t_b

$$|\Psi(t_a)\rangle = \sum_{\mu=1}^{N_{\text{ch}}} a_{\mu} |\varphi_{\mu}(t_a)\rangle \quad (2.24)$$

$$= \sum_{j=1}^{N_{\text{DVR}}} \sum_{\mu=1}^{N_{\text{ch}}} c_{j\mu} \pi_j(t_a) |\varphi_{\mu}(t_j)\rangle, \quad (2.25)$$

$$|\Psi(t_b)\rangle = \sum_{\mu=1}^{N_{\text{ch}}} b_{\mu} |\varphi_{\mu}(t_b)\rangle \quad (2.26)$$

$$= \sum_{j=1}^{N_{\text{DVR}}} \sum_{\mu=1}^{N_{\text{ch}}} c_{j\mu} \pi_j(t_b) |\varphi_{\mu}(t_j)\rangle. \quad (2.27)$$

In equations (2.24) and (2.26), $|\Psi(t_a)\rangle$ and $|\Psi(t_b)\rangle$ are expanded directly in the adiabatic basis at corresponding times. In equations (2.25) and (2.27), $|\Psi(t_a)\rangle$ and $|\Psi(t_b)\rangle$ are given in the STD expansion (see equation (2.16)). Equations (2.24) and (2.26) are now inserted

into equation (2.22) to obtain

$$\sum_{j=1}^{N_{\text{DVR}}} \sum_{\mu=1}^{N_{\text{ch}}} \left[\frac{i}{2} (D_{ij} - D_{ji}^*) O_{iv,j\mu} - \delta_{ij} \delta_{v\mu} E_v(t_i) \right] c_{j\mu} = \frac{i}{2} \pi_i^*(t_a) \sum_{\mu=1}^{N_{\text{ch}}} O_{iv,\mu}^{(a)} a_{\mu} - \frac{i}{2} \pi_i^*(t_b) \sum_{\mu=1}^{N_{\text{ch}}} O_{iv,\mu}^{(b)} b_{\mu}, \quad (2.28)$$

where

$$O_{iv,\mu}^{(a)} = \langle \varphi_v(t_i) | \varphi_{\mu}(t_a) \rangle, \quad O_{iv,\mu}^{(b)} = \langle \varphi_v(t_i) | \varphi_{\mu}(t_b) \rangle, \quad (2.29)$$

are the matrices of overlap elements between adiabatic basis functions evaluated at the quadrature abscissas, and the adiabatic basis functions evaluated at the temporal endpoints. Equation (2.28) represent the TDSE on the interval (2.9) in the STD method, and contain all the information we need to construct the STD time propagator. To see that this really is the case, and to construct the propagator explicitly, we introduce the matrices \mathbf{C} , \mathbf{A} and \mathbf{B} with dimensions $\dim(\mathbf{C}) = N_{\text{STD}} \times N_{\text{STD}}$ and $\dim(\mathbf{A}) = \dim(\mathbf{B}) = N_{\text{STD}} \times N_{\text{ch}}$ and elements given by

$$C_{iv,j\mu} = \frac{i}{2} (D_{ij} - D_{ji}^*) O_{iv,j\mu} - \delta_{ij} \delta_{v\mu} E_v(t_i), \quad (2.30)$$

$$A_{iv,\mu} = \pi_i^*(t_a) O_{iv,\mu}^{(a)}, \quad B_{iv,\mu} = \pi_i^*(t_b) O_{iv,\mu}^{(b)}. \quad (2.31)$$

The introduction of the matrices \mathbf{C} , \mathbf{A} and \mathbf{B} allows us to write equation (2.28) in the compact form

$$\mathbf{C}c = \frac{i}{2} (\mathbf{A}a - \mathbf{B}b), \quad (2.32)$$

where c is the vector of length N_{STD} composed of the coefficients $c_{j\mu}$ from equation (2.16), a and b are vectors of length N_{ch} composed of the a_{μ} and b_{μ} coefficients from equations (2.24) and (2.26), respectively. It should be noted that the way we constructed the LHS of equation (2.28), and thereby the matrix \mathbf{C} , ensures that this matrix is Hermitian and hence has an inverse. This property originates back from equation (2.18), which also ensures that the a and b vectors appears explicitly in equation (2.32).

We now project $\langle \varphi_v(t_a) |$ onto equations (2.24) and (2.25) from the left, to obtain

$$a = \mathbf{A}^{\dagger} c, \quad (2.33)$$

and $\langle \varphi_v(t_b) |$ from the left onto equations (2.26) and (2.27)

$$b = \mathbf{B}^{\dagger} c. \quad (2.34)$$

Since the matrix \mathbf{C}^{-1} exist, we can express the vector c in terms of the vectors a and b

$$c = \frac{i}{2} \mathbf{C}^{-1} (\mathbf{A}a - \mathbf{B}b). \quad (2.35)$$

Finally we insert equation (2.35) into the equations (2.33) and (2.34), and solve for b to obtain the equations:

$$b = \mathbf{U}_a a, \quad \mathbf{U}_a = \left(\mathbf{A}^{\dagger} \mathbf{C}^{-1} \mathbf{B} \right)^{-1} \left(\mathbf{A}^{\dagger} \mathbf{C}^{-1} \mathbf{A} + 2i \right), \quad (2.36)$$

$$b = \mathbf{U}_b a, \quad \mathbf{U}_b = \left(\mathbf{B}^{\dagger} \mathbf{C}^{-1} \mathbf{B} - 2i \right)^{-1} \mathbf{B}^{\dagger} \mathbf{C}^{-1} \mathbf{A}, \quad (2.37)$$

where $\dim(\mathbf{U}_a) = \dim(\mathbf{U}_b) = N_{ch} \times N_{ch}$. In equations (2.36) and (2.37) a linear operator, represented by \mathbf{U}_a or \mathbf{U}_b , is applied to the vector a to get the vector b . In the limit of results converged with respect to the number of adiabatic channels, the vectors a and b give a complete description of the initial state $|\Psi(t_a)\rangle$ and the final state $|\Psi(t_b)\rangle$, respectively (see equations (2.24) and (2.26)). Thus the matrices \mathbf{U}_a and \mathbf{U}_b represent the time propagator $U(t_b, t_a)$ in the STD formulation, which makes equations (2.36) and (2.37) the main results of this chapter.

Since the time propagators \mathbf{U}_a and \mathbf{U}_b are derived directly from the TDSE, we expect them to be unitary and equal, but for a finite basis \mathbf{U}_a and \mathbf{U}_b are generally different and non-unitary. In the limit of a complete basis in both time and space ($N_{DVR} \rightarrow \infty$ and $N_{ch} \rightarrow \infty$), it is shown in [1] that $\mathbf{U}_a = \mathbf{U}_b$ and that both time propagators are unitary. We therefore expect time propagation, carried out using the STD method, to be norm conserving and the results to be independent of whether \mathbf{U}_a or \mathbf{U}_b is used as the time propagator, as long as the results are converged with respect to N_{DVR} and N_{ch} .

2.4 Illustrative examples

In this section we present calculations carried out using the STD time propagator. The main focus is to confirm consistency of the formulation, thus we restrict ourselves to simple 1D models with time-dependent Hamiltonians of the form

$$H(t) = -\frac{1}{2} \frac{d^2}{dx^2} + V(x, t). \quad (2.38)$$

To enforce a purely discrete spectrum of this Hamiltonian, we consider the problem in a sufficiently large but finite spatial box $-X \leq x \leq X$ with zero boundary conditions for the wave function $\Psi(x, t) = \langle x | \Psi(t) \rangle$ at its end points. After a brief discussion of the implementation of the method, we consider calculations in two model systems. First, we investigate the survival probability of a hydrogen atom interacting with an intense laser field. Second, to illustrate the versatility of the STD propagator, we apply the method to a study of the elastic scattering and resonant charge-transfer processes in proton-hydrogen collisions.

2.4.1 Implementation

To propagate a solution $|\Psi(t)\rangle$ of the TDSE through an interval (2.9) by means of the propagators defined in equations (2.36) or (2.37), the matrices \mathbf{A} , \mathbf{B} , and \mathbf{C} defined by equations (2.30) and (2.31) are needed. In present calculations, the eigenstates of $H(t)$ needed to construct these matrices are calculated using the sin-DVR basis [13] (See also ref. [14]). This basis incorporates zero boundary conditions $\Psi(\pm X, t) = 0$, as can be seen from Figure A.1 in appendix A. A grid in x with spacing of 0.15 was found to be sufficient to obtain converged results for the systems considered in this section. As a temporal basis we use the Legendre-DVR basis. In principle any basis set satisfying equations (2.10)-(2.13) could be used. However, special attention should be paid to the completeness relation (2.11), since this relation must hold everywhere in the interval (2.9), including the end points t_a and t_b . This property cannot be fulfilled by e.g. the Fourier DVR basis (also referred to as a Cartesian mesh [15]) or the sin-DVR basis. For the Fourier DVR basis this is related to the fact, that the Fourier series for a function defined in the interval (2.9) converges to a function having equal values at $t = t_a$ and $t = t_b$. A similar problem is present in the sin-DVR basis, where all basis functions are zero when evaluated at the end points, and consequentially all functions expanded in this basis will have zero boundary values. The matrix elements and functions needed to construct the temporal part of the STD time propagator, are given in ref. [1].

When the matrices \mathbf{A} , \mathbf{B} , and \mathbf{C} are constructed, the main workload in the implementation of equations (2.36) and (2.37) is to invert the matrix \mathbf{C} . This is done using a standard numerical library LAPACK. The computational time of this step grows cubically with $N_{\text{STD}} = N_{\text{DVR}}N_{\text{ch}}$, which is the dimension of \mathbf{C} . In situations with strong non-adiabatic couplings between many adiabatic states, the number of adiabatic channels N_{ch} required for convergence is large. It is therefore desirable to reduce the duration of the propagation interval (2.9), such that relatively few temporal basis functions are sufficient to accurately describe the evolution of $|\Psi(t)\rangle$, since this will reduce N_{STD} . To propagate through longer intervals, the full calculation is split into propagation through N_{sec} sections. The systems we consider here are not of a nature where it is favorable to chose different sector lengths or vary the number of temporal basis functions. We therefore chose sectors of equal length, spanned by a constant number of N_{DVR} basis functions. When this is the case, the endpoint basis amplitudes $\pi_i(t_a)$ and $\pi_i(t_b)$ and the derivative matrix (2.21), needed to construct the matrices (2.30) and (2.31), are the same and should be calculated only once.

We have confirmed numerically that the propagators in equations (2.36) and (2.37) rapidly converge to each other and become unitary as N_{DVR} and N_{ch} grows. A more in depth numerical analysis of the equality and unitarity of the propagators are given in ref. [1]. The present results where obtained with $N_{\text{DVR}} = 9$; other numerical parameters used in the calculations are specified below. The convergence of the results with respect to all parameters was ensured. The absolute errors of the probabilities shown in the figures below do not exceed 10^{-4} .

2.4.2 Hydrogen atom in a pulsed laser field

We consider a one-dimensional hydrogen atom described by a soft-core Coulomb potential interacting with a pulsed laser field. In the dipole approximation and length gauge, the time-dependent potential in equation (2.38) is for this model given by

$$V(x, t) = -\frac{1}{\sqrt{x^2 + 1}} + F(t)x, \quad (2.39)$$

where

$$F(t) = F_0 \cos^2\left(\frac{\pi t}{T}\right) \sin(\omega t), \quad -\frac{T}{2} \leq t \leq \frac{T}{2}, \quad (2.40)$$

is the electric field. We report calculations of the probability P_0 to survive in the initial (field-free) ground state after the pulse is over. In the calculation of P_0 we use pulses with fixed amplitudes $F_0 = 0.1$, durations $T = 6\pi/\omega$, and frequencies ω varying from 0.035 to 0.5. To highlight the advantage of the STD propagator method in comparison with integration of the Born-Fock equations (2.7), we show in Figure 2.1 the energies $E_v(t)$ of several of the lowest adiabatic states as functions of the scaled time t/T . In this representation the adiabatic energy curves, obtained for different frequencies ω , look identical.

As seen from the figure, there is a number of avoided crossings where the functions $E_v(t)$ rapidly change their slopes, and some of them are sharply localized in time. An accurate integration of equation (2.7) through such intervals requires a very small time step, as discussed in section 2.2. The performance of the STD propagator method, on the other hand, is not affected by these avoided crossings. For example, to obtain converged results for P_0 using the STD method, in the worst case required $N_{\text{sec}} = 500$ sectors, and hence totally $9 \times 500 = 4500$ quadrature abscissas in time. In comparison the integration of equation (2.7) was still not converged to the same degree when $5 \cdot 10^5$ steps where used.

Figure 2.2 shows P_0 as a function of the pulse frequency ω . Since the field has died out at the time of evaluation, we have that $P_0 = |b_1|^2$ (see equation (2.26)). For $\omega \geq 0.1$,

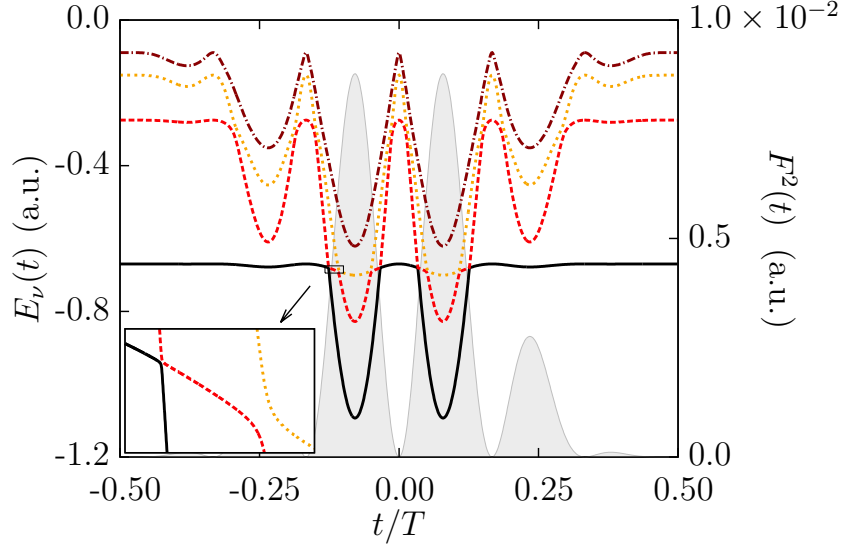


Figure 2.1: Energies of the adiabatic ground state (solid line) and three lowest excited states (dashed, dotted, and dashed-dotted lines) as functions of the scaled time for pulses (2.40) with $F_0 = 0.1$. The gray shadow shows the electric field squared (right-hand axis). The inset enlarges a region of avoided crossings.

the converged STD results were obtained using a spatial box with $X = 15$ and $N_{\text{ch}} = 20$ adiabatic channels. The whole time interval (see (2.40)) was divided into $N_{\text{sec}} = 300$ sectors. With these parameters, the calculations are rather fast. At lower frequencies, a larger spatial box with $X = 1.5\alpha$ was used, where $\alpha = F_0/\omega^2$ is the amplitude of the classical quiver motion in a monochromatic field. The number of adiabatic channels and time sectors needed for convergence gradually grows to $N_{\text{ch}} = 290$ and $N_{\text{sec}} = 500$ as ω decreases to 0.035. The need for this many adiabatic channels can be explained using an energy picture. The maximum kinetic energy of an electron accelerated in the field is $\sim F_0/2\omega^2$, so for low frequencies the wave package of ionized electrons contains very many energy components. The many energy components lead to a big spread in the spatial distribution, increasing the area where high spatial resolution is needed.

A rapid growth of computational time makes the present calculations for $\omega < 0.035$ unpractical. For comparison, Figure 2.2 also contain the survival probability P_0^{AA} obtained using the adiabatic approximation. P_0^{AA} is given by

$$P_0^{\text{AA}} = \exp\left(-\int_{-\infty}^{\infty} \Gamma_0(F(t))dt\right), \quad (2.41)$$

where $\Gamma_0(F(t))$ is the ionization rate in a static electric field with the field strength $F(t)$. The ionization rate is found using the technique developed in ref. [16].

The STD results in Figure 2.2 demonstrate a non-monotonic behavior at $\omega \gtrsim 0.1$. The structures can be understood in terms of multiphoton resonance conditions between the field-free eigenstates of the atom. For example, the local minimum of P_0 at $\omega \approx 0.4$ reflects a one-photon resonance between the ground state ($E_0 \approx -0.670$) and first excited state ($E_1 \approx -0.275$). For $\omega \lesssim 0.1$ the survival probability P_0 decreases monotonically with ω and approaches the adiabatic result. The condition of validity of the adiabatic approximation is that the time scales of the field and the field-system-interaction is much longer then

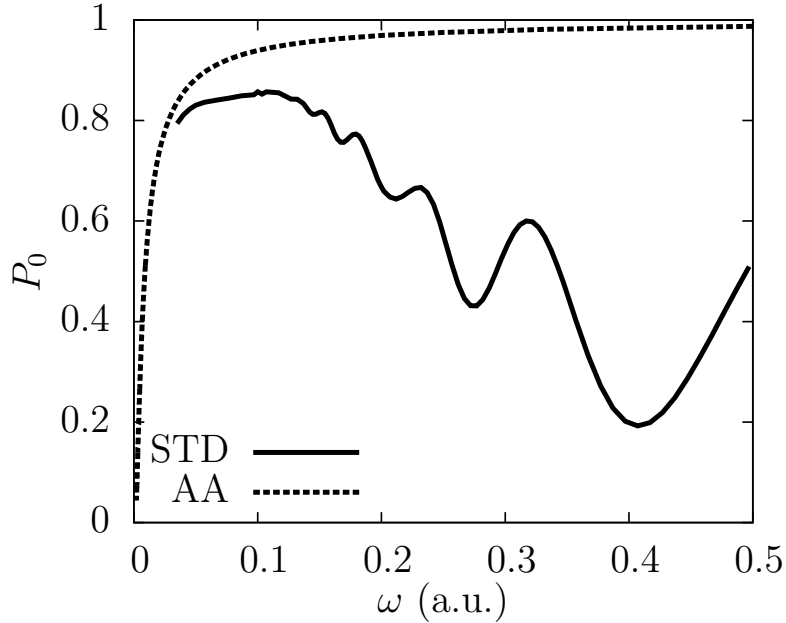


Figure 2.2: Probability to survive in the initial ground state P_0 for pulses (2.40) with $F_0 = 0.1$ as a function of the pulse frequency. *Solid line*: converged STD results. *Dashed line*: the adiabatic approximation given in equation (2.41).

the intrinsic time scale of the system. In the presence of a weak-field ($F_0 \ll 1$) this is the case when $\omega \ll F_0^2/|E_0|(E_1 - E_0) \approx 0.04$ [17]. We therefore expect the STD result and the adiabatic approximation to converge for $\omega < 0.04$, although we cannot fully confirm this in the present calculations of P_0 .

The low frequency regime is generally very difficult to treat in direct numerical calculations because of the exceedingly high order laser-atom coupling. Disregarding this notoriously difficult region, the discussion above and Figure 2.2 shows that the STD propagator method is efficient and yields accurate results over a broad dynamical range from the tunneling to the multi-photon regime.

2.4.3 Proton-hydrogen collisions

We next consider a one-dimensional model of proton-hydrogen collisions. In this model the time-dependent potential of equation (2.38) is given by

$$V(x, t) = - \left(\frac{1}{\sqrt{(x - vt/2)^2 + 1}} + \frac{1}{\sqrt{(x + vt/2)^2 + 1}} \right). \quad (2.42)$$

The electron-proton interaction is again described by a soft-core Coulomb potential. The protons are assumed to move with constant velocities $\pm v/2$, and to be localized at $x = \pm R/2$ at the initial moment $t = -T/2$, where $R = vT/2$ is the initial distance between the two protons. During the time T each of the two protons move to the initial position of the other. The electron is initially bound on the left proton moving with velocity $+v/2$, forming a model hydrogen atom in a moving frame. The initial condition for the wave function is $\Psi(x, -T/2) = \varphi_0(x + R/2)e^{+ivx/2}$, where $\varphi_0(x)$ is the ground state wave function in the

soft-core Coulomb potential centered at $x = 0$ and the exponent is the electronic (Galilean) translation factor [12].

After the time propagation, when the two protons are again localized at $x = \pm R/2$, the probability of elastic scattering P_{el} and resonant charge transfer P_{ct} are extracted by projecting $\Psi(x, +T/2)$ onto $\varphi_0(x - R/2)e^{+ivx/2}$ and $\varphi_0(x + R/2)e^{-ivx/2}$, respectively. To put it another way; P_{el} is the probability that the electron remains in the ground state of the potential it was originally located on, which has now moved from the left side ($x = -R/2$) to the right side ($x = +R/2$), and P_{ct} is the probability for the electron to be in the ground state of the other potential.

We report calculations for velocities v varying from 0.1 to 2. All calculations are performed with $R = X$, which was found to be sufficient for convergence. In Figure 2.3, the energies $E_\nu(t)$ of the four lowest adiabatic states are shown as functions of vt . In this representation the adiabatic energy curves look identical for different velocities v . The adiabatic states in the present model can be classified into even (gerade) and odd

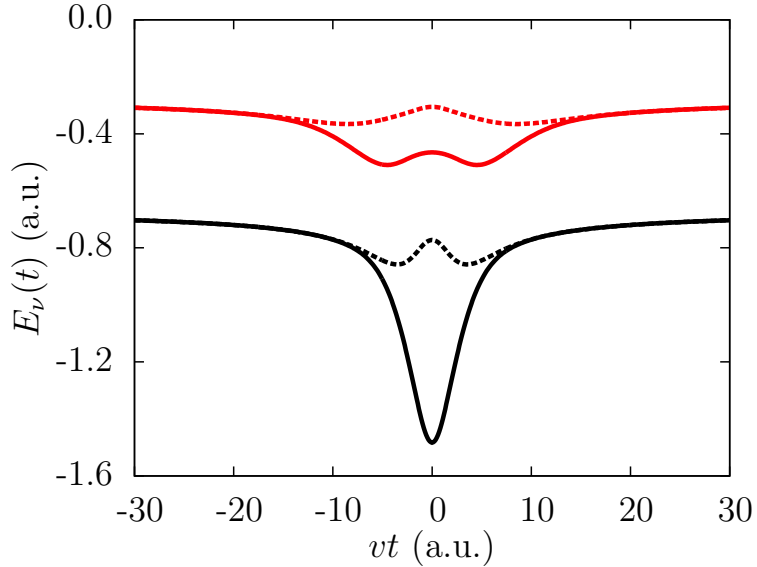


Figure 2.3: Energies of the four lowest adiabatic states in the potential (2.42) as functions of vt . The even and odd states are shown by solid and dashed lines, respectively. The lowest two (black) curves show the energies $E_g(t)$ and $E_u(t)$ of equation (2.44).

(ungerade) with respect to the reflection $x \rightarrow -x$. At large internuclear separation, the even and odd states become pairwise degenerate. This pairwise degeneracy can be seen in Figure 2.3 noting that the internuclear separation is given by $|vt|$.

Before we present the results of P_{el} and P_{ct} obtained using the STD method, we focus on a theoretical description of the proton-hydrogen collision in the adiabatic limit of $v \ll \kappa = \sqrt{2|E_0|}$. In this limit all channels of excitation and ionization are closed, and transfer of population between the two potentials are only possible through resonance charge transfer between the two ground states. The adiabatic theory of resonance charge transfer was originally developed by Firsov [18]. In this theory, the probabilities of elastic scattering $P_{\text{el}}^{\text{AA}}$ and charge transfer $P_{\text{ct}}^{\text{AA}}$ are given by

$$P_{\text{el}}^{\text{AA}} = \cos^2(\Delta), \quad P_{\text{ct}}^{\text{AA}} = \sin^2(\Delta), \quad (2.43)$$

where

$$\Delta = \frac{1}{2} \int_{-\infty}^{\infty} [E_g(t) - E_u(t)] dt. \quad (2.44)$$

Here $E_g(t)$ and $E_u(t)$ are the energies of the even (*gerade*) and odd (*ungerade*) adiabatic states converging to the initial ground states at large internuclear separations. These energies are shown by the two lowest curves in Figure 2.3. For the present model $\Delta = A/2v$, where A is the velocity-independent area between the energy curves $E_g(t)$ and $E_u(t)$ (see Figure 2.3). Hence the probabilities (2.43) as functions of v^{-1} oscillate with constant frequency. In Figure 2.4 we present the STD results for P_{el} and P_{ct} together with the adiabatic approximations $P_{\text{el}}^{\text{AA}}$ and $P_{\text{ct}}^{\text{AA}}$.

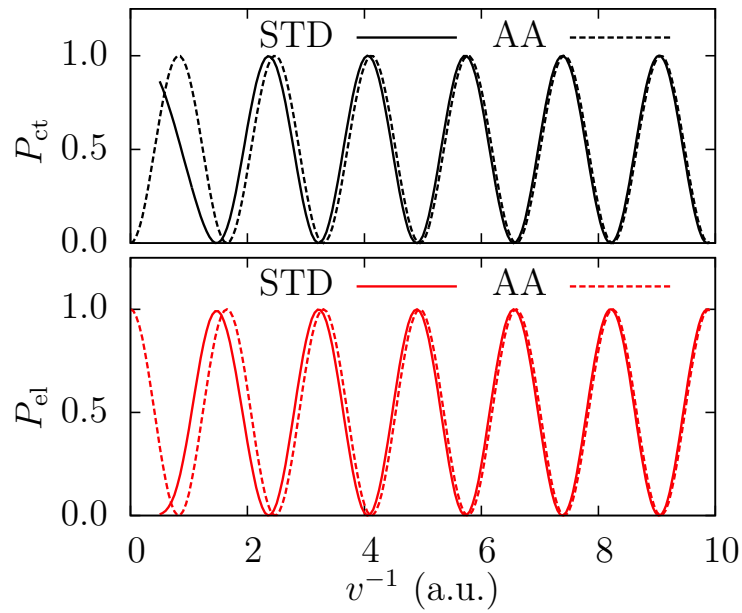


Figure 2.4: Probabilities of resonance charge transfer P_{ct} (upper panel) and elastic scattering P_{el} (lower panel) as functions of v^{-1} . *Solid lines*: converged STD results. *Dashed lines*: adiabatic approximations.

It is seen from Figure 2.4 that the adiabatic approximation works very well at low collision velocities $v^{-1} \gtrsim 4$. In this region $P_{\text{el}} + P_{\text{ct}} \approx 1$, which confirms that all inelastic processes but resonance charge transfer are suppressed. At higher velocities, $v^{-1} \lesssim 2$, excitation and ionization processes become important and the two-channel approximation of ref. [18] breaks down. At low impact velocities, the fundamental physics of the system can be understood in terms of a few adiabatic states. The number of adiabatic states needed for convergence of P_{el} and P_{ct} therefore increases from $N_{\text{ch}} = 80$ at $v = 0.1$ to $N_{\text{ch}} = 360$ at $v = 2.0$. Low impact velocities, on the other hand, result in long propagation times $T = 2R/v$ and the number of temporal sections needed for convergence decreases from $N_{\text{sec}} = 900$ at $v = 0.1$ to $N_{\text{sec}} = 300$ at $v = 2.0$.

The results of this section demonstrate that the STD propagator method is efficient and accurate also for the description of atomic collisions in a broad range of collision velocities.

2.5 Conclusion

The STD expansion of a solution $|\Psi(t)\rangle$ to the TDSE, allow us to construct an algebraic representation of the time propagator. When the system under consideration is slowly, or rather smoothly, evolving in time, the STD time propagation scheme is very efficient and versatile. The essence of the STD expansion is to expand $|\Psi(t)\rangle$ in a temporal DVR basis before treating any spatial degrees of freedom. In this way we obtain a time propagator which does not contain any of the non-adiabatic coupling terms, which made the Fock-Born equations unsuitable for numerical calculations. In the STD method we expand spatial variables in an adiabatic basis, but any complete basis could be used. However, the adiabatic basis leads to a particularly simple form of the \mathbf{C} matrix and thereby of the time propagator.

Attosecond Transient Absorption Spectroscopy

3.1 Introduction

Interaction between laser-light and matter leads to a time-dependent polarization in the material, and consequently new field components are generated. In *transient absorption spectroscopy* (TAS) the modification of a (probe) pulse, is found by measuring the intensity spectrum of the pulse, after it has propagated through a target region. When the measured spectrum is compared with the initial spectrum of the pulse, absorption and emission of laser-light can be identified. Often an additional (pump) pulse is used to get temporal resolution, in the sense described in chapter 1. The central ideas in TAS has been used for many years (see e.g. ref. [19]), but only on time scales much longer than the ones we want to consider here. In the last few years pulses of attosecond duration have been available, and with them the possibility of temporal resolution on the natural time scale of most electron dynamics. We will refer to TAS using attosecond probe pulses as *attosecond transient absorption spectroscopy* (ATAS). Since the very late 00's ATAS has been recognized as a powerful tool to study electron dynamics in atomic systems. Examples hereof are observation of valence electron motion in krypton ions [20], autoionization in Argon [21] and observation of AC Stark shift of excited states in Helium [22]. In these experiments pump pulses in the near-infrared (NIR) region has been used. These NIR pump pulses are often (parts) of the pulses used in the production of the attosecond probe pulses, and they can therefore have much higher intensities than the probe pulses. Consequentially, the attosecond pulses are often in the perturbative regime, while the pump pulses are associated with many-photon processes. As we will see, it is advantageous if the pump and probe pulses have well separated frequency profiles, but the theoretical paper ref. [23], shows that ATAS with attosecond pump pulses should also be possible.

Even though ATAS has proved itself a very efficient and reliable method to follow electron dynamics in atoms, we do not know of any experiments or theoretical papers considering ATAS in molecules. It is therefore interesting to investigate the influence of nuclear motion on the ATAS intensity spectrum. As a reference we carry out calculations on a H_2^+ -model with a fixed internuclear distance. Results from this model will be compared to calculations using a similar system, but with moving nuclei. To simplify the calculations we consider only systems of one spatial dimension and we treat the laser pulses as classical fields.

In section 3.2 we introduce a series of approximations, which allow us to set up the theory needed to calculate the ATAS intensity spectrum. Section 3.3 shortly present some numerical considerations of the actual calculations done in sections 3.3.1 and 3.3.2 for fixed

and moving nuclei models, respectively. Finally section 3.4 concludes this chapter.

3.2 Theory

To find the time-dependent polarization, introduced by the laser-field, we have to solve the TDSE. For simple systems this can be done using standard approaches, but the polarization of the system have an effect on the further propagation of the pulse, so we have to solve the Maxwell equations simultaneously. This simultaneous solution of the TDSE and Maxwell equations is a very difficult task [24]. Different approximations and simplifications can be made to minimize the difficulties in connection with propagation effects. In ref. [25] they for example assume that the polarization of the target is proportional to the electric field strength of the probe pulse. This assumption leads to Beers law. We use a different approach, as we assume that the target region is very thin, corresponding to a laser-target interaction limited to one point in space. It may seem like a very crude approximation, for the atomic gas usually used in experiments, but we do not expect the characteristics of the intensity spectrum to be affected by the propagation effects we neglect. This expectation is confirmed by ref. [26] in the case of atomic Helium, for field parameters similar to the ones we use in our calculations.

In the case of current interest, the propagation of a laser field $E(x, t)$ is governed by the scalar wave equation [23]

$$\left(\frac{\partial^2}{\partial x^2} - \frac{1}{c^2} \frac{\partial^2}{\partial t^2} \right) E(x, t) = \frac{4\pi}{c^2} \frac{\partial^2}{\partial t^2} \delta(x) P(t). \quad (3.1)$$

To obtain equation (3.1) we have used that $P(x, t) = \delta(x)P(t)$ in the thin target approximation, where $P(t)$ is the time-dependent polarization, defined as the dipole moment per length of the target region.

We assume that the incoming field $E_{\text{in}}(t - x/c)$, consisting of pump and probe pulses, is propagating undamped in the positive x direction. The total electric field then has the form

$$E(x, t) = E_{\text{in}}\left(t - \frac{x}{c}\right) + E_{\text{gen}}(x, t), \quad (3.2)$$

where $E_{\text{gen}}(x, t)$ is the field generated by the polarization in the target. We further assume that only the incoming field contribute to the polarization of the target. This assumption and the assumption that the incoming field propagates undamped, are only valid if the generated field is much weaker than the incoming field. This is the case if the target gas is dilute.

Equation (3.1) can be solved analytically for the generated field $E_{\text{gen}}(x, t)$ of equation (3.2). The solution is

$$E_{\text{gen}}(x, t) = -\frac{2\pi}{c} \left[\theta(x) \frac{\partial}{\partial t} P\left(t - \frac{x}{c}\right) + \theta(-x) \frac{\partial}{\partial t} P\left(t + \frac{x}{c}\right) \right]. \quad (3.3)$$

We see from equation (3.3) that the generated field has two components. One is propagating in the negative x direction, and one is propagating in the positive x direction. The intensity spectrum of the field (3.2) can be expressed as

$$\begin{aligned} S(\omega) &\propto \left| \int_{-\infty}^{\infty} E(x, t) \exp(i\omega t) dt \right|^2 \\ &= |E_{\text{in}}(\omega)|^2 + 2\text{Re} [E_{\text{in}}^*(\omega) E_{\text{gen}}(\omega)] + |E_{\text{gen}}(\omega)|^2 \end{aligned} \quad (3.4)$$

where $E_{\text{in}}(\omega)$ and $E_{\text{gen}}(\omega)$ are given by the Fourier transformations

$$E_{\text{in}}(\omega) = \int_{-\infty}^{\infty} E_{\text{in}}\left(t - \frac{x}{c}\right) \exp(i\omega t) dt, \quad (3.5)$$

$$\begin{aligned} E_{\text{gen}}(\omega) &= \int_{-\infty}^{\infty} E_{\text{gen}}(x, t) \exp(i\omega t) dt \\ &= \frac{2\pi\omega n}{c} \int_{-\infty}^{\infty} d(t) \exp(i\omega t) dt. \end{aligned} \quad (3.6)$$

Here n is the dipole density, and $d(t)$ is the time-dependent single-molecule dipole moment. Equation (3.6) is obtained from (3.3) by partial integration, assuming that the polarization dies out as $t \rightarrow \pm\infty$ ¹. Further, only the part of the field (3.3) propagating in the positive x direction is kept in equation (3.6). This corresponds to an experiment where the detector is placed at $x \rightarrow \infty$. As we discussed briefly, the theory we develop in this section is only reasonable when the incoming field is much stronger than the generated field. The dominant term in equation (3.4) is therefore $|E_{\text{in}}(\omega)|^2$, but this term does not contain any information about the system. We therefore subtract $|E_{\text{in}}(\omega)|^2$ from (3.4), and note that the term $|E_{\text{gen}}(\omega)|^2$ is very small. The dominant term in the remaining spectrum is

$$S_{\text{ATAS}}(\omega) \propto 2\text{Re} [E_{\text{in}}^*(\omega) E_{\text{gen}}(\omega)]. \quad (3.7)$$

We will refer to equation (3.7) as the ATAS spectrum. In the case of well separated frequency profiles of pump and probe pulses, equation (3.7) allows us to determine the modification of the probe pulse, using only information about the single-molecule dipole moment and the incoming field. The reason why the frequency profiles of the two pulses have to be well separated, is that we want a clear distinction between processes initiated by the probe pulse or pump and probe pulses combined, and the processes initiated by the pump pulse alone. For this reason we also have to put restrictions on the intensity of the pulse with the lowest frequency (most often the pump pulse). High intensities leads to high-order processes, with frequency components of much higher energies than the individual photons, and in some cases these can be confused with processes initiated by the pulse with higher frequency (most often the probe pulse). The pump pulse used in the calculations presented in section 3.3.1 has an intensity well outside the perturbative regime, but the intensity is low enough for the processes initiated by the pulse to be limited to few-photon processes.

The ATAS spectrum of equation (3.7) can be both positive and negative. If $S_{\text{ATAS}}(\omega)$ is positive when evaluated at a specific ω , the overall intensity spectrum (see equation (3.4)) has a higher intensity at that frequency. This means that light is emitted at frequencies corresponding to a positive $S_{\text{ATAS}}(\omega)$. On the other hand light is absorbed at frequencies corresponding to a negative $S_{\text{ATAS}}(\omega)$.

3.3 Implementation and Results

To obtain the ATAS spectrum of equation (3.7) we need to find the time-dependent dipole moment. In a homo-nuclear molecule with only one electron, this is given by

$$d(t) = -\langle x \rangle, \quad (3.8)$$

where $\langle x \rangle$ is the expectation value of the position of the electron found at time t . $d(t)$ is found by solving the TDSE for H_2^+ , with either fixed or moving nuclei, in the presence of the pump and probe pulses. The quantum state describing the internal dynamics of the H_2^+ molecule is a function of one spatial variable for fixed nuclei and two spatial variables

¹We will return to this assumption in section 3.3

for moving nuclei. For such low dimensions, the split-step method originally proposed in ref. [4] is very efficient and precise. The results presented in this chapter has been calculated using a numerical implementation of the fast Fourier transformation split-step method, made by Lun Yue. For details about the implementation, the choice of coordinates and explicit expressions for the potentials see ref. [27].

To obtain the ATAS spectrum, we take the Fourier transformation of the incoming field (see equations (3.5) and (3.7)). To minimize artificial effects from the envelope function, we will in this chapter only use pulses with Gaussian envelope functions. For a pulse of finite duration, propagating in vacuum, it is required by the Maxwell equations that the vector potential $A(t) = -\int dt E(t)$ vanishes at $t \rightarrow \pm\infty$ [28]. This requirement is automatically fulfilled by e.g. the field (2.40) used in chapter 2, because the product of envelope and carrier functions is anti-symmetric under the reflection $t \rightarrow -t$. Using a similar approach, we could construct a field with a Gaussian envelope which satisfies the Maxwell equations. However, if we want to control e.g. the carrier-envelope phase δ , we have to use the more general approach of constructing the electric field from the vector potential

$$A(t) = \frac{\varepsilon(t)}{\omega} \cos[\omega(t - t_c) + \delta], \quad (3.9)$$

with an envelope function $\varepsilon(t)$ centered around t_c

$$\varepsilon(t) = \exp\left[-\frac{(t - t_c)^2}{\tau^2}\right], \quad \tau = \frac{N_{\text{cycles}}\pi}{\omega\sqrt{\ln(2)}} \quad (3.10)$$

where N_{cycles} is the number of cycles of the carrier function in equation (3.9) within the FWHM of the Gaussian envelope. From this point on, when we talk about an N -cycle pulse we refer to an electric field defined through equation (3.9) and (3.10), with $N_{\text{cycle}} = N$. Since $E(t) = -\partial_t A(t)$, the electric field corresponding to the vector potential in equation (3.9) contains two terms, but the pulse is still centered around t_c with ω as the dominant frequency component. For all calculations presented in this section, we choose $\delta = 0$.

3.3.1 Fixed nuclei calculations

In Figure 3.1 we show the single-molecule dipole moment as a function of time, when a single 3-cycle pulse with wavelength $\lambda = 90$ nm, is applied to the H_2^+ -model with fixed nuclei. For more parameters of this field, see appendix A.2. We immediately notice from Figure 3.1 that the dipole moment $d(t)$ is present a long time after the pulse has died out. When the pulse is gone, the system is left in a superposition of field-free eigenstates of the Hamiltonian of the system. The time evolution of this superposition is governed by the trivial time evolution of the individual field-free eigenstates. Consequentially, $d(t)$ will after the pulse consist of terms oscillating with frequencies corresponding to the energy difference between populated eigenstates. Since spontaneous emission is not included in our model, these oscillating terms will never die out. The central energy of the pulse used in Figure 3.1 was 13.8 eV, and it primarily transferred population to a state 10.0 eV above the ground state. An energy difference of 10.0 eV corresponds to a term oscillating with a period of 410 as.

In the remainder of this chapter, I will refer to the non-zero dipole moment, present after the pulse has died out, as the dipole tail. In Figure 3.1 this corresponds to the region where $d(t)$ has a well defined frequency. The dipole tail constitutes a numerical problem, since we have to take the Fourier transformation of the time-dependent dipole moment (see equations (3.7) and (3.6)). However, the tail is also very important for the spectral resolution of the ATAS spectrum. If this tail was not present, the high temporal resolution following from the short probe pulse, will result in low spectral resolution. The tail of $d(t)$, ensures that high temporal *and* spectral resolution can be obtained simultaneous in

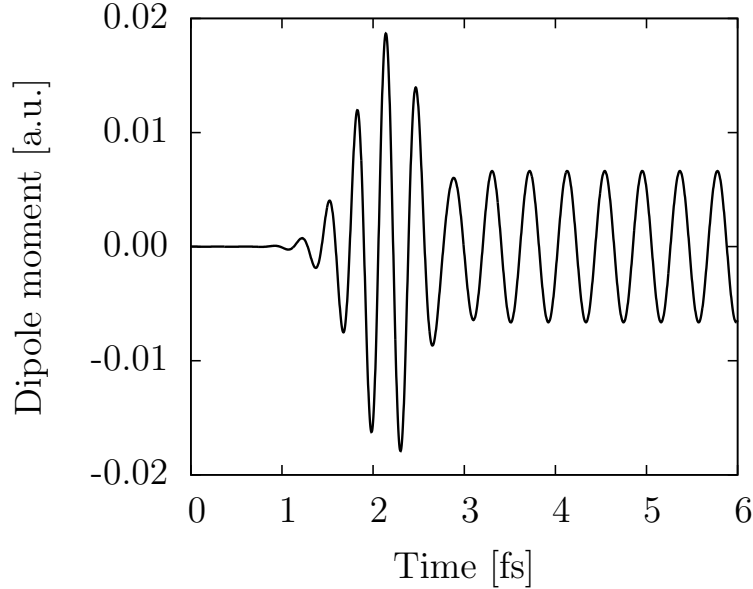


Figure 3.1: The dipole moment in 1D H_2^+ with fixed nuclei as a function of time, when a single pulse is applied. The pulse is present from ~ 1.5 fs to ~ 2.5 fs.

ATAS spectra by extending the time a target responds to an incoming pulse. It is natural to compare our model with Nature, where spontaneous emission damps the tail of $d(t)$ on a nanosecond time scale [29]. Spontaneous emission results in an exponential decay of the dipole moment, but it turns out that the spectrum is not very sensitive to the actual form of the damping, as long as the damping-function is smooth and damps the dipole moment on a time scale much longer than the time scale of the molecular dynamics. In our numerical calculations we use a modified version of the Hann window function [30] to damp $d(t)$.

Figure 3.2 shows the ATAS spectrum for 1D H_2^+ with fixed nuclei for different values of the time delay between pump and probe pulses. The pump pulse used is a long 700 nm pulse while the probe pulse is a much shorter 50 nm pulse. See appendix A.2 for a complete list of field parameters. In the ATAS spectrum of Figure 3.2, positive delays correspond to the situation where the pump arrives before the probe. For delays $\tau \gtrsim 8$ fs, the pump pulse arrives at the target well before the probe pulse. For the field parameters considered here, the pump pulse is not energetic enough to excite the system out of its ground state. The pump pulse will therefore not have any effect on the ATAS spectrum when $\tau \gtrsim 8$ fs. The two peaks seen in Figure 3.2 for $\tau \gtrsim 8$ therefore correspond to resonances in the un-dressed system. The potential of the field-free system is symmetric around $x = 0$, and the eigenstates of the field-free Hamiltonian can therefore be classified as even (gerade) or odd (ungerade) under the reflection $x \rightarrow -x$. The laser transition between two states of same symmetry is dipole-forbidden, and therefore suppressed compared to transitions between states of different symmetry². The two peaks in Figure 3.2 correspond to transitions between the gerade ground state and two ungerade states with energies 21.48 eV and 25.29 eV above the ground state energy.

For $\tau \lesssim -15$ fs the probe pulse arrives well before the pump pulse. When the pump arrives, some excited states have already been populated. The pump pulse will not change

²Note the extremely low intensity of the probe pulse.

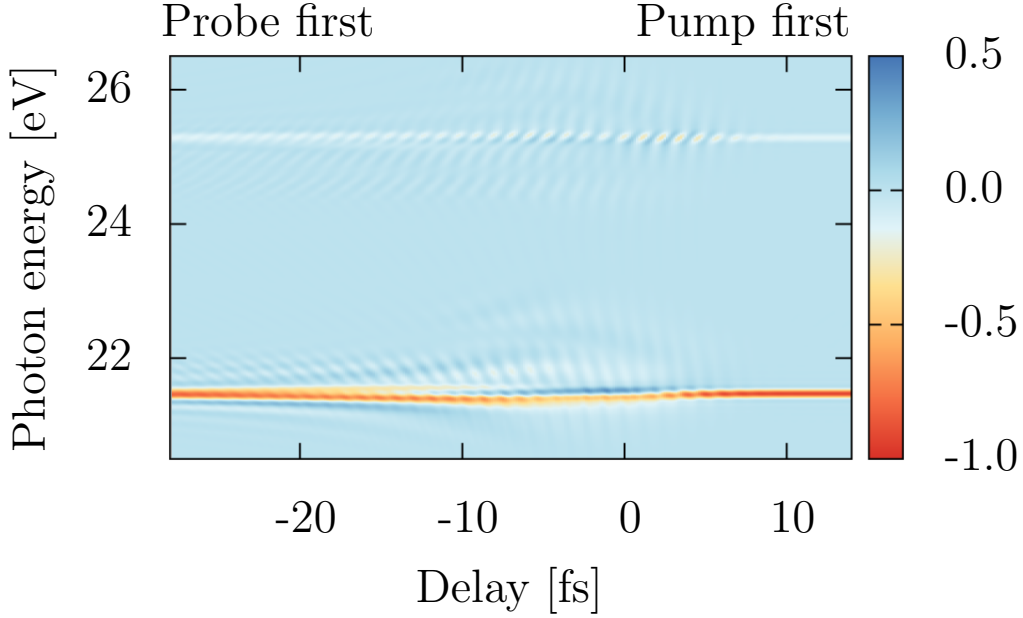


Figure 3.2: Normalized ATAS spectrum (see equation (3.7)) for one-dimensional H_2^+ with fixed nuclei. For pulse parameters see appendix A.2.

the population of these excited states, but it can affect the dipole tail. This is presumably the reason for the small side-bands and oscillations in the $\tau \lesssim -15$ fs region. The region $-15 \text{ fs} \lesssim \tau \lesssim 8 \text{ fs}$ is very interesting, since the temporal overlap of pump and probe pulses leads to large modifications of the ATAS spectrum. In this region we see a small shift in the absorption peaks, a clear splitting of the lower absorption peak, and several new peaks. The dynamics in this region are dominated by intense coupling between individual states. It is a subject of current investigation whether the splitting of the lower absorption peak can be classified as an Autler-Townes splitting [31]. In the region $-15 \text{ fs} \lesssim \tau \lesssim 8 \text{ fs}$ we find traces of so called *Light-induced states* (LIS) [24]. The LIS of interest here are due to second order processes involving one photon from the pump pulse and one photon from the probe pulse. These two-photon transitions occurs between states of same symmetry, and only when the pump and probe pulses overlap in time. The signature of these LIS in the ATAS spectrum, are absorption peaks placed one pump-photon energy from the energy of a gerade state. Such a peak should be visible in Figure 3.2 at ~ 22.1 eV corresponding to the energy of a nearby gerade state (23.87 eV) minus the energy of a pump-photon. There is a peak in this region, but strong interaction between different states makes it difficult to exclude that this peak is due to other processes. In Figure 3.3, however, we see a clear peak at ~ 19.4 eV corresponding to the gerade state (17.65 eV) plus the energy of a pump-photon. Calculations where the central wavelength of pump laser has been changed, confirms that the peak at ~ 19.4 is indeed a signature of a LIS.

The absorption peak corresponding to the LIS at ~ 19.4 eV has a periodic modulation (see Figure 3.3). The period of this modulation corresponds to half a pump pulse period.

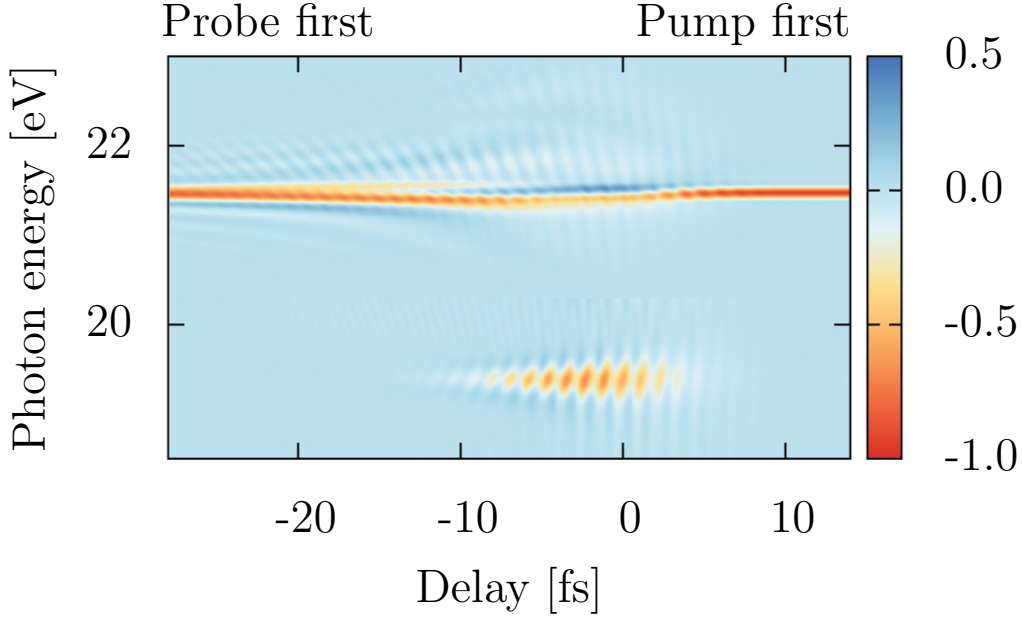


Figure 3.3: Normalized ATAS spectrum (see equation (3.7)) for one-dimensional H_2^+ with fixed nuclei. For photon energies lower than 20.3 eV, the intensities has been multiplied by a factor of 50 to highlight the LIS.

Effects similar to this modulation are described in ref. [24], by considering a few-state-model. The tilt of the fringes in the absorption peak is a subject of current investigation.

3.3.2 Moving nuclei calculations

In section 3.3.1 we saw that a long tail in the time-dependent dipole moment $d(t)$, made it possible to achieve high spectral resolution, even when our probe pulse was very short. For H_2^+ with moving nuclei we find that $d(t)$ behaves very differently from the way it did in the fixed nuclei case. Figure 3.4 shows two examples of $d(t)$ calculated for 1D H_2^+ with moving nuclei, when a single pulse is applied.

The left hand side of Figure 3.4 shows a dipole moment, with a tail much smaller than the contribution to $d(t)$ from the region where the pulse is on (pulse region). Consequentially, $d(t)$ is almost antisymmetric around the middle of the pulse at ~ 2.1 fs. In the pulse region, the distribution of frequency components of the dipole moment is very similar to the distribution of frequency components in the field. Therefore, when $d(t)$ is dominated by contributions from the pulse region, the ATAS spectrum contain mainly information about the field. However, when a very short pulse is used, the tail of $d(t)$ will again be dominant over contributions from the pulse region, see the right hand side of Figure 3.4. The pulse used in the calculations of the data presented in the right hand side of Figure 3.4, has a central energy of 41.3 eV which is well above the ionization energy of

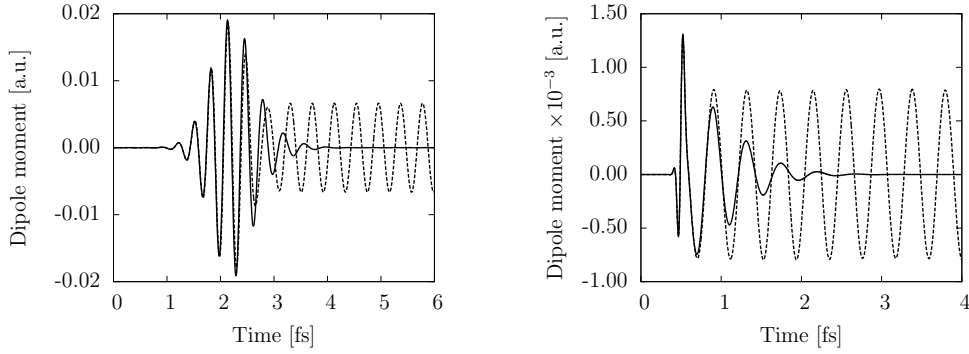


Figure 3.4: The dipole moment in 1D H_2^+ with moving nuclei (full lines) and in 1D H_2^+ with fixed nuclei (dashed lines) as functions of time, when a single pulse is applied. *Left*: Same 90 nm 3-cycle pulses as in Figure 3.1. *Right*: A much shorter 30 nm 1-cycle pulse. For a full list of pulse parameters, see appendix A.2.

29.6 eV³. Anyway, only the first excited state, 10.0 eV above the ground state energy, is substantially populated. That only the first excited state is substantially populated can be seen from the tail of $d(t)$, which oscillates with a period of approximately 410 as (see section 3.3.1) just after the pulse is over. For later times the period of oscillation becomes longer, which indicates that the energy difference between ground state and first excited state becomes smaller. The damping of the dipole tail happens on a sub-femtosecond time scale. Such fast damping, will lead to several eV broad peaks in the ATAS spectrum. The reason for the damping is a subject of current research, but it is definitely a consequence of dissociation of the populated excited state(s).

We now conclude, that ATAS spectra with the spectral resolution of the ones in section 3.3.1 are impossible, or at least very difficult, to achieve for 1D H_2^+ with moving nuclei. The temporal resolution in the spectra is also reduced by the very broad absorption peaks. On the other hand, the dipole signal resulting from a single pulse contains temporal information on its own. The oscillations of the dipole tail depend exclusively on the ratio between populations of states. We have found that ultra short pulses near or above the ionization threshold primarily populate the first excited state, and since the tail is the dominant contribution to the dipole moment for such short pulses, we expect the corresponding ATAS spectrum to be independent of pulse parameters. In Figure 3.5 we compare three ATAS spectra each using a single ultra short pulse, of central energy 20, 30 or 40 eV. For a full list of pulse parameters see appendix A.2.

We see from Figure 3.5 that the width of the absorption peak at ~ 10 eV is almost constant for the three different pulse energies. We therefore claim that the width of this peak is a measure of the time it takes $d(t)$ to decay, and that this time is related to the time it takes the first excited state to dissociate. We return to the interpretation of this *dissociation time* in chapter 4. The small shift of the absorption peak at ~ 10 eV, is a consequence of the small dipole contribution from the pulse region. Assuming an exponential damping of dipole tail and a Lorentzian lineshape of the peak in Figure 3.5, the width of the absorption peak corresponds to a lifetime⁴ of ~ 600 as.

³For the equilibrium distance of the nuclei.

⁴Time it takes for the damping function to fall off by a factor of e^{-1}

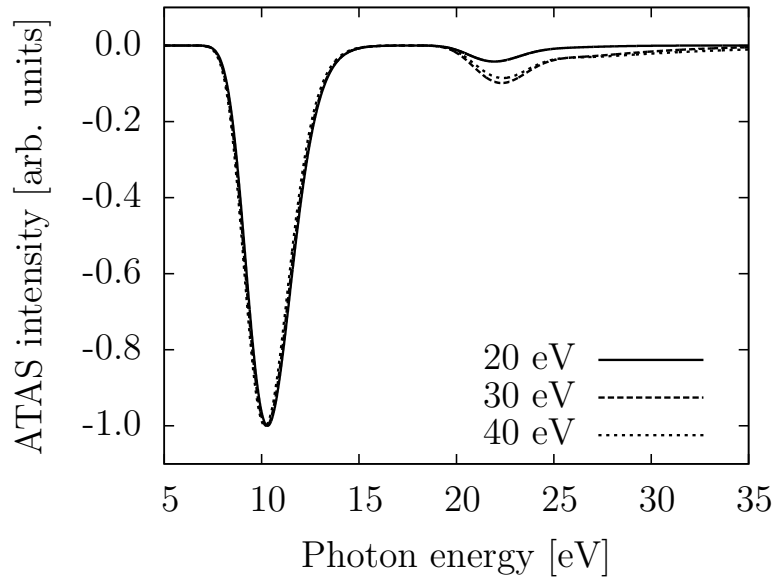


Figure 3.5: The single pulse ATAS spectrum for three ultra short pulses with different central energies. The ATAS spectra has been normalized to have the same peak value. For a full list of pulse parameters see appendix A.2.

3.4 Conclusion

We have seen that it is possible to get very detailed temporal and spectral information from ATAS spectra of H_2^+ with fixed nuclei, using a very simple theoretical approach. The assumptions made in the theoretical model are crude, but they should be compatible with experiments. For calculations with moving nuclei, we found that the pump-probe approach could no longer give the desired resolution. However, the temporal information in the time-dependent dipole moment, indicates that the dissociation time of the first excited state in H_2^+ can be found from the ATAS spectrum using a single ultra short pulse. Whether this method can be used to determine the dissociation time of excited states in larger molecules is still an open question.

Further plans

This chapter contains further plans for my Ph.D. studies. Special attention will be given to possible extensions, improvements, combinations, and interpretations of the two theories introduced and discussed in chapters 2 and 3.

The STD method of chapter 2 was validated by calculations on one-dimensional systems with only one electron, but the extension to more complicated systems seems straightforward. The only difference is that the adiabatic states used as spatial basis, are functions of more variables. However, this leads to a computational problem as the stationary problem of finding the adiabatic states has to be solved for very many times (See section 2.4). For the simple systems considered in section 2.4 this was not a problem, since it took less than a tenth of a second to solve the time-independent problem for a given set of field parameters. For larger systems, the situation is different and we have to come up with a new approach if we want to use the STD method in an efficient way. A promising approach is to solve the time-independent problem in the Kramers-Henneberger frame [32]. In this frame the effect of an external field is 'absorbed' in the electron-nucleus interaction(s) by modified electron-nucleus distance(s). All other terms in the Hamiltonian are left as if there was no field. As a consequence, the adiabatic states for non-vanishing fields, can be found from the field-free states by a spatial shift. This method has already been applied to one-dimensional two electron systems in electric fields, to make an efficient implementation of the STD method. Going to higher dimensionalities causes some numerical difficulties. Nevertheless, this way of finding adiabatic states might save the prospects of using the STD method on systems of higher dimensionalities, and make it an interesting tool for further research.

In section 3.3.2 we stated that an ATAS spectrum of H_2^+ with moving nuclei, obtained using only a single laser pulse, gave information about the dissociation time of the first excited state. Here we shortly look into the reasoning behind this statement and how it can be validated or improved. The results in section 3.3.2 indicated that only the two eigenstates $|\Phi_1(x, R)\rangle$ and $|\Phi_2(x, R)\rangle$ of the full Hamiltonian were populated for times after the laser pulse. In the Born-Oppenheimer approximation, these two states are given by the products

$$|\Phi_j(x, R)\rangle = F_j(R)|\varphi_j(x, R)\rangle, \quad j = 1, 2, \quad (4.1)$$

where $\varphi_j(x, R)$ are the j 'th electronic state, found for fixed values of the internuclear distance R , and $F_j(R)$ are the nuclear wave package corresponding to the j 'th electronic state (See e.g. ref. [29]). In the Born-Oppenheimer approximation, the damping of the time-dependent dipole moment is controlled by the spatial overlap of $F_1(R)$ and $F_2(R)$, and since the ground state is bound, we expect the damping of $d(t)$ to be a consequence of the dissociation of the nuclear wave package $F_2(R)$ alone. The interpretation of dipole

damping and thereby the width of the ATAS peaks, is therefore straight forward in the Born-Oppenheimer approximation. However, it is by no means certain that the Born-Oppenheimer approximation applies to the system we consider here. The timescale of electronic motion (oscillation period of ~ 400 as) is not that much faster than the nuclear motion (Lifetime of ~ 600 as), and the validity of the Born-Oppenheimer approximation should be tested. One way to perform such a test, is to do a calculation where several electronic contributions $|\varphi_i(x, R)\rangle$ are considered in the expansion of each state $|\Phi_j(x, R)\rangle$. Results of this calculation should be compared to the results obtained using the Born-Oppenheimer approximation. Such a test is a part of my current studies.

Even though new methods might be needed for the calculation of the adiabatic states, it would also be a very interesting project to use the STD method for time evolution in the calculation of ATAS spectra. To develop new methods and ideas, Lars and I have discussed the possibility of going abroad for 3 months.

Discrete Variable Representation (DVR)

In this appendix, a basis with the properties given in equations (2.10)-(2.13), will be constructed and described. Such a basis is referred to as a DVR basis. For simplicity we only consider real DVR functions in this appendix, but the results are easily generalized to complex functions.

A.1 A short introduction to the DVR basis

From the set of N_{DVR} polynomials $\{p_k(z) | k = 0, \dots, N_{\text{DVR}} - 1\}$, where $p_k(z)$ is a polynomial of order k , orthogonal on the interval $z \in [z_a, z_b]$

$$\int_{z_a}^{z_b} \omega(z) p_k(z) p_l(z) dz = h_k \delta_{kl}, \quad (\text{A.1})$$

the normalized polynomials

$$\tilde{P}_k(z) = \sqrt{\frac{\omega(z)}{h_k}} p_k(z), \quad (\text{A.2})$$

are introduced. For a discrete approximation of an integral, we use the N_{DVR} -point quadrature rule [33]

$$\int_{z_a}^{z_b} \omega(z) F(z) dz \simeq \sum_{i=1}^{N_{\text{DVR}}} \omega_i F(z_i), \quad (\text{A.3})$$

where $F(z)$ is an arbitrary function and ω_i and z_i are the quadrature weights and abscissas, respectively. Standard procedures for finding the quadrature weights and abscissas exists [30], so we will not consider their evaluation here. Equation (A.3) is exact for polynomials of degree $2N_{\text{DVR}} - 1$ or less, which leads to the two expressions

$$\int_{z_a}^{z_b} \tilde{P}_k(z) \tilde{P}_l(z) dz = \sum_{i=1}^{N_{\text{DVR}}} \frac{\omega_i}{\omega(z_i)} \tilde{P}_k(z_i) \tilde{P}_l(z_i) = \delta_{kl}, \quad (\text{A.4})$$

$$\int_{z_a}^{z_b} \tilde{P}_k(z) z \tilde{P}_l(z) dz = \sum_{i=1}^{N_{\text{DVR}}} \frac{\omega_i}{\omega(z_i)} z_i \tilde{P}_k(z_i) \tilde{P}_l(z_i) \equiv z_{kl}. \quad (\text{A.5})$$

By introducing the $N \times N$ matrix \mathbf{T} with elements

$$T_{ni} = \sqrt{\frac{\omega_i}{\omega(z_i)}} \tilde{P}_{n-1}(z_i), \quad n = 1, 2, \dots, N_{\text{DVR}} \quad (\text{A.6})$$

we can restate equations (A.4) and (A.5) as

$$\mathbf{T}\mathbf{T}^\dagger = \mathbf{T}^\dagger\mathbf{T} = \mathbf{1} \quad (\text{A.7})$$

$$\mathbf{T}\mathbf{z}_D\mathbf{T}^\dagger = \mathbf{z}, \quad (\text{A.8})$$

where \mathbf{z}_D is a $N \times N$ diagonal matrix with the quadrature abscissas as eigenvalues. The interpretation of equation (A.7) is clear; the matrix \mathbf{T} is unitary, and can therefore be used as a unitary transformations matrix. Equation (A.8) tells us that if we use this transformation on the original basis of orthonormal polynomials, we obtain a basis in which the \mathbf{z} matrix is diagonal

$$\mathbf{T}^\dagger\mathbf{z}\mathbf{T} = \mathbf{z}_D. \quad (\text{A.9})$$

The functions obtained by transforming the orthonormal polynomials are referred to as DVR functions, and the set of DVR functions is referred to as the DVR basis. Because all basis vectors are real, and the transformation is unitary, the relation between the orthonormal polynomials $\tilde{P}_k, k = 0, \dots, N_{\text{DVR}} - 1$ and the DVR functions $\tilde{\pi}_i, i = 1, \dots, N_{\text{DVR}}$ are

$$\tilde{\pi}_i(z) = \sum_{n=1}^{N_{\text{DVR}}} T_{ni} \tilde{P}_{n-1}(z) \quad , \quad \tilde{P}_{n-1}(z) = \sum_{i=1}^{N_{\text{DVR}}} T_{ni} \tilde{\pi}_i(z). \quad (\text{A.10})$$

The original basis of orthonormal polynomials satisfies equations (2.10) and (2.11), and since the transformation is unitary, these properties will carry over to the DVR basis. We now show that the DVR basis also satisfy equations (2.12) and (2.13).

$$\begin{aligned} \tilde{\pi}_i(z_j) &= \sum_{n=1}^{N_{\text{DVR}}} T_{ni} \tilde{P}_{n-1}(z_j) \\ &= \sum_{n=1}^{N_{\text{DVR}}} T_{ni} T_{nj} \sqrt{\frac{\omega(z_j)}{\omega_j}} \\ &= \sum_{n=1}^{N_{\text{DVR}}} T_{in}^\dagger T_{nj} \sqrt{\frac{\omega(z_j)}{\omega_j}} \\ &= \delta_{ij} \sqrt{\frac{\omega(z_i)}{\omega_i}} \end{aligned} \quad (\text{A.11})$$

From first to second line we used (A.6), and to obtain the final result the unitarity of the transformation matrix was used. From the property (A.11) and the N_{DVR} -point Gaussian quadrature rule, it is straight forward to show that (2.13) is satisfied by the DVR basis vectors

$$\begin{aligned} \int_{z_a}^{z_b} \tilde{\pi}_i(z) F(z) \tilde{\pi}_j(z) dz &\simeq \sum_{k=1}^{N_{\text{DVR}}} \frac{\omega_i}{\omega(z_k)} \tilde{\pi}_i(z_k) F(z_k) \tilde{\pi}_j(z_k) \\ &= \sum_{k=1}^{N_{\text{DVR}}} \delta_{ik} \delta_{jk} F(z_k) \\ &= \delta_{ij} F(z_i) \end{aligned} \quad (\text{A.12})$$

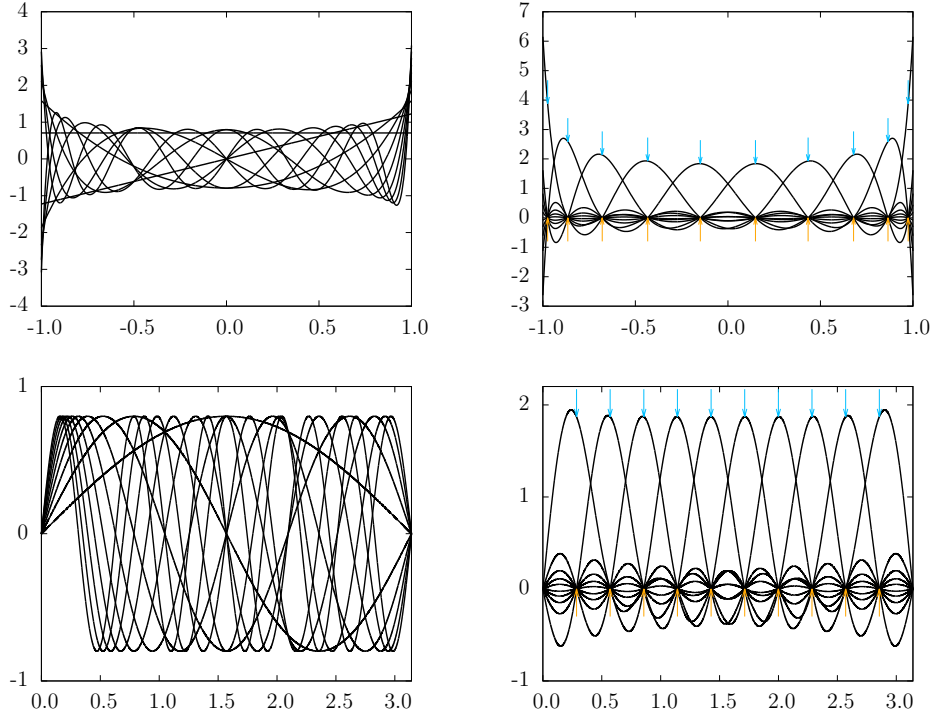


Figure A.1: *Upper left*: The ten lowest Legendre polynomials on their interval of orthogonality. *Lower left corner*: The ten lowest sine functions on their interval of orthogonality. *Right side*: the DVR functions corresponding to the functions on the left. Orange arrows indicates the quadrature abscissas, and the blue arrows the factor $\sqrt{\omega(z_i)}/\omega_i$.

The approximation in (A.12) is introduced by the Gaussian quadrature rule, since the function $F(z)$ is in general not a polynomial of degree one or less. When a set of DVR functions have been constructed on the interval $z \in [z_a, z_b]$, it is easy to transform the functions and corresponding matrix elements to a general interval $t \in [t_a, t_b]$. In Figure A.1 we show two examples of DVR bases; The Legendre- and the sin-DVR¹. The Legendre DVR basis will be used as temporal basis in the STD method, and the sin-DVR basis will be used to construct the adiabatic bases used in this method. It is important to note that the sin-DVR incorporates zero boundary conditions, while the Legendre-DVR basis is complete (in the sense of equation (2.11)) everywhere on the interval $z \in [z_a, z_b]$.

A.2 Field parameters

In this section we give the field parameters used in the calculations producing data for the figures in chapter 3. λ is the central wavelength of the pulse; the wavelength of the carrier function. E_{pulse} is the central energy of the pulse; the frequency of the carrier function. N_{cycles} are the number of laser cycles in the pulse (see section 3.3). Finally T_{pulse} is the pulse period given by the FWHM of the envelope function.

¹Note that the construction of the sin-DVR differs a little from the one described above. The reason is that the sine basis is not a set of polynomials.

Field parameters for Figure 3.1	
λ	90 nm
E_{pulse}	13.8 eV
N_{cycles}	3
T_{pulse}	900 as
I	10^{11} W/cm ²

Field parameters for Figure 3.2 and Figure 3.3		
	Pump pulse	Probe pulse
λ	700 nm	50 nm
E_{pulse}	1.77 eV	24.8 eV
N_{cycles}	6	2
T_{pulse}	14.0 fs	330 as
I	2×10^{12} W/cm ²	5×10^7 W/cm ²

Field parameters for Figure 3.4		
	Left figure	Right figure
λ	90 nm	30 nm
E_{pulse}	13.8 eV	41.3 eV
N_{cycles}	3	1
T_{pulse}	900 as	100 as
I	10^{11} W/cm ²	10^{11} W/cm ²

Field parameters for Figure 3.5			
	First (20 eV) pulse	Second (30 eV) pulse	Third (40 eV) pulse
λ	62.0 nm	41.3 nm	31.0 nm
E_{pulse}	20.0 eV	30.0 eV	40.0 eV
N_{cycles}	1	1	1
T_{pulse}	207 as	137 as	103 as
I	10^{11} W/cm ²	10^{11} W/cm ²	10^{11} W/cm ²

Bibliography

- [1] Bækhoj J. E., Tolstikhin O. I., and Madsen L. B. (2014) *J. Phys. B: At. Mol. Opt. Phys.* 47, 075007.
- [2] Hentschel M. et al. (2001) *Nature* 414, 509.
- [3] Crank J. and Nicolson P. (1947) *Math. Proc. Camb. Phil. Soc.* 43, 50.
- [4] Feit M. D., Fleck Jr J. A., and Steiger A. (1982) *J. Comput. Phys.* 47, 412.
- [5] Tal-Ezer H. and Kosloff R. (1984) *J. Chem. Phys.* 81, 3967.
- [6] Park T. J. and Light J. C. (1986) *J. Chem. Phys.* 85, 5870.
- [7] Kienberger R. et al. (2004) *Nature* 427, 817.
- [8] Eckle P. et al. (2008) *Nature Physics* 4, 565.
- [9] Griffiths D. J. (2005) Introduction to quantum mechanics, second edition, Pearson Prentice Hall, Upper Saddle River NY.
- [10] Tolstikhin O. I., Watanabe S., and Matsuzawa M. (1996) *J. Phys. B: At. Mol. Opt. Phys.* 29, L389.
- [11] Born M. and Fock V. (1928) *Z. Phys.* 51, 165.
- [12] Landau L. D. and Lifshitz E. M. (1977) Quantum mechanics, third edition, Butterworth-Heinemann, Burlington MA.
- [13] Muckerman J. T. (1990) *Chem. Phys. Lett.* 173, 200.
- [14] Colbert D. T. and Miller W. H. (1992) *J. Chem. Phys.* 96, 1982.
- [15] Peng L. (2005) Ph.D. thesis: Dynamics of Diatomic Molecules in Intense Fields, Department of Applied Mathematics and Theoretical Physics, The Queen's University Belfast, Belfast, Northern Ireland.
- [16] Batishchev P. A., Tolstikhin O. I., and Morishita T. (2010) *Phys. Rev. A* 82, 023416.
- [17] Tolstikhin O. I. and Morishita T. (2012) *Phys. Rev. A* 86, 043417.
- [18] Firsov O. B. (1951) *Zh. Eksp. Teor. Fiz.* 21, 1001.
- [19] Porter G. and Topp M. R. (1968) *Nature* 220, 1228.
- [20] Goulielmakis E. et al. (2010) *Nature* 466, 739.
- [21] Wang H. et al. (2010) *Phys. Rev. Lett.* 105, 143002.
- [22] Chini M. et al. (2012) *Phys. Rev. Lett.* 109, 073601.

- [23] Baggesen J. C., Lindroth E., and Madsen L. B. (2012) *Phys. Rev. A* 85, 013415.
- [24] Gaarde M. B., Buth C., Tate J. L., and Schafer K. J. (2011) *Phys. Rev. A* 83, 013419.
- [25] Santra R., Yakovlev V. S., Pfeifer T., and Loh Z. (2011) *Phys. Rev. A* 83, 033405.
- [26] Chen S. et al. (2012) *Phys. Rev. A* 86, 063408.
- [27] Yue L. (2014) Part A thesis: Strong Field Dissociation and Ionization of H_2^+ , Department of Physics and Astronomy, Aarhus University, Aarhus, Denmark.
- [28] Madsen L. B. (2002) *Phys. Rev. A* 65, 053417.
- [29] Bransden B. H. and Joachain C. J. (2003) *Physics of atoms and molecules*, second edition, Pearson Education, Harlow, England.
- [30] Press W. H., Teukolski S. A., Vetterling W. T. and Flannery B. P. (1992) *Numerical Recipes in FORTRAN*, second edition, Cambridge University Press, Cambridge, England.
- [31] Autler S. H. and Townes C. H. (1955) *Phys. Rev.* 100, 703.
- [32] Henneberger W. C. (1968) *Phys. Rev. Lett.* 21, 838.
- [33] Abramowitz M. and Stegun I. A. (1972) *Handbook of mathematical functions*, Courier Dover Publications, Dover, England.